Multi-Valley Electron Conduction at the Indirect-Direct Crossover Point in Highly-Tensile-Strained Germanium

M. B. Clavel[1], F. Murphy-Armando[2*], Y. Xie[3], K. T. Henry[4], M. Kuhn[4], R. J. Bodnar[5], G. A. Khodaparast[3], D. Smirnov[6], J. J Heremans[3], and M. K. Hudait[1*]

[1]*Advanced Devices & Sustainable Energy Laboratory (ADSEL), Bradley Department of Electrical and Computer Engineering, Virginia Tech, Blacksburg, Virginia 24061, USA*

[2]*Tyndall National Institute, University College Cork, Lee Maltings, Dyke Parade, Cork, Ireland*

[3]*Department of Physics, Virginia Tech, Blacksburg, Virginia 24061, USA*

[4]*Intel Corporation, Hillsboro, Oregon, USA*

[5]*Fluids Research Laboratory, Department of Geosciences, Virginia Tech, Blacksburg, Virginia 24061, USA*

[6]*National High Magnetic Field Laboratory, Tallahassee, Florida 32310, USA*

As forward-looking electron devices increasingly adopt high-mobility, low-bandgap materials, such as germanium (Ge), questions remain regarding the feasibility of strain engineering in low-bandgap systems. Particularly, the Ge *L*–Γ valley separation (~150 meV) can be overcome by introducing a high degree of tensile strain (ε ≥ 1.5%). It is therefore essential to understand the nature of highly-strained Ge transport, wherein multi-valley electron conduction becomes a possibility. Here, we report on the competitiveness between *L* and Γ valley transport in highly tensile strained (ε ~ 1.6%) Ge/$In_{0.24}Ga_{0.76}As$ heterostructures. Temperature-dependent magnetotransport analysis revealed two contributing carrier populations, identified as lower- and higher-mobility *L* and Γ valley electrons (in Ge) using temperature-dependent Boltzmann transport modeling. Coupling this interpretation with electron cyclotron resonance studies, the effective mass (m^*) of the higher-mobility Γ valley electrons was probed, revealing $m^* = (0.049 \pm 0.007)m_e$. Moreover, comparison of the empirical and theoretical m^* indicated that these electrons reside primarily in the first two quantum sublevels of the Ge Γ valley. Consequently, our results provide insight into the strain-dependent carrier dynamics of Ge, offering new pathways toward efficacious strain engineering.

PhySH: *Semiconductors, Narrow Band Gap Systems, Molecular Beam Epitaxy, Transport Phenomena, Cyclotron Resonance, Density Functional Theory, Boltzmann Theory*

Date Received: September 24, 2020

I. INTRODUCTION

Epitaxial and process-induced strain have been used to enhance the electronic transport properties of silicon (Si) metal-oxide-semiconductor field-effect transistors (MOSFETs) for over a decade [1,2]. In particular, silicon-germanium ($Si_{1-x}Ge_x$) alloy source-drain stressors [3,4] and virtual substrates [5] have been utilized to apply compressive strain to the Si channel in *p*-MOSFETs, enhancing hole mobility in proportion to the Si/$Si_{1-x}Ge_x$ lattice mismatch (*i.e.*, strain, ε). More recently, narrow bandgap semiconductors, such as germanium (Ge) and III-V ternary alloys (*e.g.*, $In_xGa_{1-x}As$), have attracted significant attention due to their enhanced electron and hole mobilities as compared to Si [6–10]. Similar to Si-based FET architectures, epitaxial and process-induced strain have also been proposed as methods for enhancing the electronic transport properties of high-mobility semiconductors [11,12]. Whereas current research has predominately focused on the demonstration of strained Ge (or $In_xGa_{1-x}As$) FETs [13–15], comparatively little effort [16] has been dedicated to elucidating the effects of high strain-states on the electronic transport properties of strained Ge (ε-Ge) materials. Moreover, the difficulty of such an investigation is compounded by Ge's pseudo-direct bandgap nature, wherein only a ~150 meV difference separates the *L* and Γ valley conduction band minima [11,17–19]. Thus, at high strain-states (ε ≥ 1.5%) [18,19], strain-induced modification of the Ge band structure is expected to lower the Γ valley conduction band minimum below that of the *L* valley, thereby transitioning Ge into a direct bandgap material with the potential for competitive behavior between the two conduction band minima to arise [20, 21]. However, the density of states (DOS) mass in the *L* and Γ valley without strain are $m_L^{DOS} = 0.22\, m_e$ and $m_\Gamma^{DOS} = 0.05\, m_e$ at room temperature, respectively (m_e denotes the free-electron mass). The DOS mass in the *L* valley does not change appreciably and the Γ valley DOS mass reduces from $0.05\, m_e$ at 0% strain to $0.04\, m_e$ at 1.6% biaxial tensile strain. Therefore, the carriers can presumably stay within the *L* valley, and by increasing doping along with tensile strain, one can transfer the carriers from the *L* valley to Γ valley. To achieve the carrier transport through Γ valley, it needs to be separated in energy from *L* valley by several tens of meV. The decoupling of carrier density and mobility from these two valleys as a function of biaxial tensile strain is still elusive to date, especially the enhancement of the mobility for *L* electrons. By applying biaxial tensile strain of ~ 1.6%, the indirect bandgap Ge converts to direct bandgap, demonstrated theoretically using ***k.p*** and experimentally [21-

23] by low temperature photoluminescence and photoreflectance measurements. At this strain level, the electrons with high mobility can begin to populate the Γ valley and thus decoupling of carriers and their mobility is a significant challenge. Thus, the strained enhanced mobility in ε-Ge and relative proportion of carriers in each valley as a function of strain and temperature are of importance. This transport study can find several applications; where carrier density, band offset for carrier confinement and strain level which enhance mobility, all needed for low power tunnel transistor [24, 25], tunnel FET based memory and logic devices [26, 27], laser [21, 28-30], spintronics [31, 32] and qubit [33] applications. In addition, there could be an application in single electron and quantum devices as well as in cryoelectronic, in which the Γ electron participation studied here is relevant.

In order to shed light onto these issues, this work exploits the ability of group IV/III-V heterostructures to induce modular, tunable epitaxial stress in Ge thin-films provided by underlying III-V strain stressor [25, 34, 35], thereby enhancing the electronic transport properties of the strained epitaxial Ge layers in a controlled fashion. Utilizing dual chamber, vacuum interconnected molecular beam epitaxy (MBE) system, we demonstrate the feasibility of integrating low-defect, atomically-abrupt tensile strained ε-Ge/$In_xGa_{1-x}As$ heterostructures on lattice-mismatched (001)GaAs substrates. Further characterization of the thin-film ε-Ge electronic transport properties and an independent, combined first-principles and Boltzmann transport calculation framework reveal directly multi-valley (*i.e.*, *L* and Γ valleys) conduction in the ε-Ge material system. The temperature dependence of the calculated mobility and carrier contributions in *L* and Γ valley of ε-Ge were compared with the experimental measured results. We also present the direct probing of carrier effective mass in ε-Ge under biaxial tensile stress, and from these results, provide new evidence for the transition from indirect to direct bandgap in tensile strained Ge thin-films.

II. METHODS

A. Material Synthesis and Characterization

The unintentionally doped epitaxial unstrained Ge/AlAs and tensile strained Ge/$In_xGa_{1-x}As$ (0.75% and 1.6%) heterostructures were grown using an *in-situ* dual-chamber MBE growth process. Separate III-V and IV reactors connected *via* an ultra-high vacuum transfer chamber allowed for isolated growth phases for the $In_{0.24}Ga_{0.76}As$ (AlAs, $In_{0.16}Ga_{0.84}As$) and unstrained Ge or ε-Ge layers, thereby minimizing the likelihood of atomic interdiffusion at the ε-Ge/$In_{0.24}Ga_{0.76}As$ heterointerface (or ε-Ge/$In_{0.16}Ga_{0.84}As$) as well as during ε-Ge growth. The initial (001)GaAs substrate was offcut 2° towards the ⟨110⟩ direction and desorbed of native oxide at 750°C under an arsenic (As) overpressure of ~10^{-5} Torr. Here, the (100)/2° GaAs substrate was used for efficient strain relaxation of the graded $In_xGa_{1-x}As$ buffer layer, which is important for subsequent ε-Ge layer growth. The substrate offcut along with growth parameters (*i.e.*, growth temperature, growth rate, grading rate, substrate conductivity, *etc*) are used to relax the strain energy from the $In_xGa_{1-x}As$ graded buffer to create a virtual substrate (or template) for subsequent layer growth. Reflection high-energy electron diffraction was used to analyze the surface before, during, and after growth. In the case of 1.6% ε-Ge sample, 0.25 µm of GaAs was grown at 650°C, followed by a 1 µm linearly graded $In_xGa_{1-x}As$ buffer and the 500 nm $In_{0.24}Ga_{0.76}As$ stressor grown at 550°C. The ultra-thin 30 nm ε-Ge layer was grown at 400°C using a 0.025 µm/hr growth rate in order to maintain heterointerface abruptness. The growth temperature and growth rate for all other Ge samples were kept constant. Complete details of the growth procedure can be found elsewhere [25]. **Table I** shows each Ge/III-V heterostructure studied in this work.

Table I. Information on the unstrained Ge/AlAs and tensile strained Ge/$In_{0.16}Ga_{0.84}As$, Ge/$In_{0.24}Ga_{0.76}As$ heterostructures.

Heterostructure	Strain (%)	Ge Thickness (nm)
Ge/AlAs/(100)2° GaAs	0	270
Ge/$In_{0.16}Ga_{0.84}As$/$In_xGa_{1-x}As$/(100)2° GaAs	0.75	15
Ge/$In_{0.24}Ga_{0.76}As$//$In_xGa_{1-x}As$/(100)2° GaAs	1.6	30

Subsequent characterization of the heterostructure's crystal quality, empirical $In_xGa_{1-x}As$ stressor composition, and epilayer relaxation and strain-states was accomplished using high-resolution x-ray diffraction (HR-XRD). The x-ray rocking curves and reciprocal space maps were recorded using a PANalytical X-pert Pro system equipped with PIXcel and proportional detectors and a monochromatic Cu Kα (λ = 1.540597 Å) x-ray source. A JY Horiba LabRam HR800 system equipped with a 514.32 nm Ar laser source was used for the collection of Raman spectra and independent corroboration of the ε-Ge epitaxial strain. Atomic force microscopy (AFM) micrographs collected with a Bruker Dimension Icon AFM in tapping mode were utilized to analyze the surface morphology of the ε-Ge/$In_{0.24}Ga_{0.76}As$ heterostructure. Further structural characterization by way of high-resolution cross-sectional transmission electron microscopy (HR-TEM) was performed on a JEOL 2100 TEM and revealed the structural quality, ε-Ge/$In_{0.24}Ga_{0.76}As$ heterointerface uniformity, and lattice coherence at the strained layer/stressor heterointerface. Additional atomic-scale characterization of the ε-Ge/$In_{0.24}Ga_{0.76}As$ interface was performed *via* atomic probe tomography (APT), a combination of time-of-flight spectroscopy and atomic projection imaging that allows for

the reconstruction of atomically-accurate three-dimensional (3-D) ion maps of selected regions of material. Optimization of the measurement conditions utilized herein began by cooling of the sample to 50 K, followed by a reduction of the laser pulse energy to 3 pJ at a pulse frequency of 250 kHz. The resultant detection rate, approximately 0.01 ions/pulse, was maintained throughout the analysis. We note that the analysis was performed parallel to the ⟨001⟩ growth direction. The commercially-available IVAS™ software was used in the reconstruction of the 3-D ion maps.

B. Electronic and Magnetotransport Analysis

The unstrained and highly tensile strained Ge magnetotransport properties, including carrier density and mobility, were measured using Hall measurement under the van der Pauw geometry. InSn Ohmic contacts were alloyed on the Ge surface to ensure low-resistance, stable electrical contacts at cryogenic temperatures. Temperature-dependent magnetotransport measurements were performed from 0.36 K to 5.63 K in magnetic fields up to ± 9 T using a ^{3}He cryostat and liquid ^{3}He submersion and sample-in-vapor cooling. Carrier effective masses for the ε-Ge/$In_{0.24}Ga_{0.76}As$ heterostructure were extracted from the temperature dependence of Shubnikov–de Haas oscillations in magnetotransport data and independently confirmed *via* electron cyclotron resonance analysis. The magnetotransmission measurements necessary for probing the cyclotron resonance response of the ε-Ge/$In_{0.24}Ga_{0.76}As$ heterostructure were carried out at the National High Magnetic Field Laboratory using a Fourier-transform infrared spectrometer, superconducting magnet, Globar emission source, and Si bolometer detector.

C. Calculation of the Ge Electronic Transport Properties Under Tensile Stress

The electronic and band structure properties of the ε-Ge/$In_xGa_{1-x}As$ heterostructures were theoretically investigated using first-principles calculations that included the effect of strain on Ge material properties. The calculations follow the approach taken by one of the authors for the calculation of transport in SiGe alloys and strained Ge nanostructures, with the addition of changes to the proportion of transport in each valley due to the presence of the InGaAs layer, as explained below. The resulting material parameters were used with the Boltzmann transport equation to determine the *n*-type carrier mobility in the ε-Ge layers and examine the population distribution of carriers between the *L* and Γ valleys of Ge. The electron-phonon scattering matrix elements in the ε-Ge were calculated using first-principles density functional perturbation theory (DFTP) for inter-valley scattering and the frozen phonon approach for intra-valley scattering by acoustic phonons, as in Ref. [20, 36] for strained Ge and SiGe. The effects of ionized impurity scattering are included using the Brooks-Herring approach [37–40]. To ease integration of the transport properties across the Brillouin zone at different strain conditions, we used the first-principles-based **k·p** analytic form of the electronic band structure of ε-Ge after Rideau *et al*. [17]. This **k.p** approach, unlike the Local Density Approximation in DFT, gives the correct electronic energy gap and dispersion. We correct the temperature dependence of the energy gap and dispersion following the approach of ref. [37] for strained SiGe (including Ge). The temperature and alloy content dependent mobility of $In_xGa_{1-x}As$ was obtained from reported experimental values [41].

The effects of quantum confinement follow an envelope function approach [42], with the boundary conditions given by the empirical ε-Ge/$In_xGa_{1-x}As$ band offsets reported in ref. [25]. To simplify the calculation, we approximated the heterostructure by a mirror-symmetric InGaAs/Ge/InGaAs structure, rather than the uncapped case of the experiment. Due to the large band offsets, this approximation allows for much faster computation with little sacrifice to accuracy. The presence of air rather than InGaAs at one end would shift the wavefunction slightly towards the InGaAs, due to the larger Ge/Air band offset. Because the wavefunction in the InGaAs region is so small, we expect the effect on the mobility to be very small.

The contribution to the mobility from the Ge *L* and Γ valleys and the $In_xGa_{1-x}As$ Γ valley was given by:

$$\mu_{Ge/In_{0.24}Ga_{0.76}As} = r_{InGaAs}\mu_{InGaAs} + r_{Ge}^{\Gamma}\mu_{Ge}^{\Gamma} + r_{Ge}^{L}\mu_{Ge}^{L}, \quad (1)$$

where μ_i^j is the calculated contribution to the mobility from material *i* and valley *j*, and r_i^j is the proportion of carriers in valley *j* of material *i*, given by:

$$r_i^j = n^j / n_T \sum_b \int_i dz \left|\psi_b^j(z)\right|^2, \quad (2)$$

where $\psi_b^j(z)$ is the z direction part of the separable envelope wavefunction of sub-band *b* of valley *j*, and the integral only runs in coordinate z inside material *i*. Coordinate *z* denotes the growth and confinement direction. The number of carriers in valley *j* is n^j , out of a total of $n_T = n^{Ge} + n^{InGaAs}$ carriers.

III. RESULTS

A. Structural Properties and Relaxation Dynamics of the ε-Ge/$In_{0.24}Ga_{0.76}As$ System

A cross-sectional schematic diagram of the ε-Ge/$In_{0.24}Ga_{0.76}As$ heterostructure investigated herein is presented in the left inset of Fig. 1(a). Similarly, the right inset of Fig. 1(a) illustrates the impact of epitaxially-induced tensile strain on the (expanded) in-plane and (compressed) out-of-plane lattice constants, *a* and *c*, respectively, of a coherently-strained epilayer (*i.e.*, $a_{epi} = a_{stressor}$). When utilizing $In_xGa_{1-x}As$ as a stressor, tailoring of the InAs mole

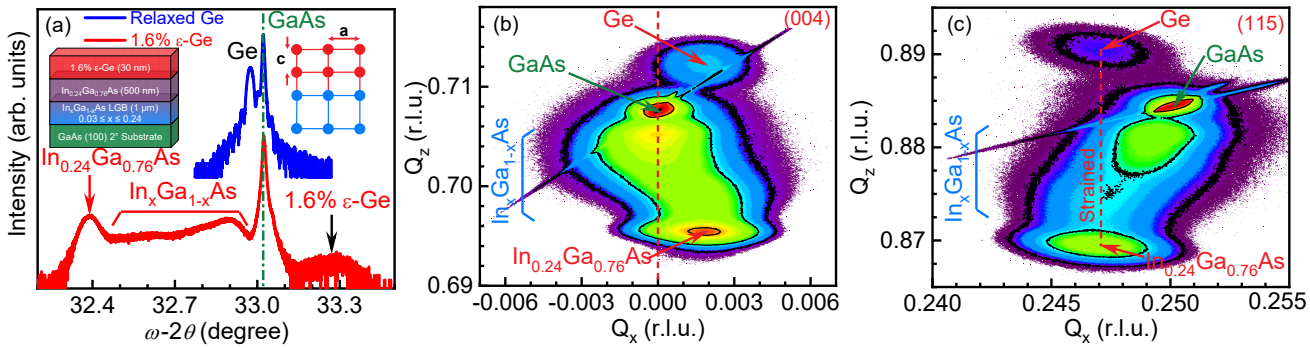

FIG. 1. (a) Symmetric (004) ω-2θ HR-XRD spectra of the as-grown ε-Ge/$In_{0.24}Ga_{0.76}As$ heterostructure (red), as compared to a quasi-lattice-matched Ge/GaAs(001) heterostructure (blue). The right inset demonstrates the out-of-plane lattice contraction due to corresponding in-plane lattice expansion, whereas the left inset provides a cross-sectional schematic of the ε-Ge/$In_{0.24}Ga_{0.76}As$ heterostructure. High-resolution reciprocal space maps taken along the (b) symmetric (004) and (c) asymmetric (115) crystallographic orientations.

fraction, and therefore $a_{In_xGa_{1-x}As}$, enables modulation of the lattice strain imparted to an overlying lattice-mismatched film, *e.g.*, Ge. In turn, the electronic and optical properties of the overlying strained epilayer can be tuned within a wide range by varying the amount of strain. As such, a target InAs mole fraction of 0.24 was selected for this work, corresponding to a nominal ~1.63% tensile strain with respect to relaxed Ge. Such a high Ge strain state has been predicted to lower the Ge Γ valley conduction band minimum below that of the *L* valley, resulting in a direct bandgap Ge material [11,12,18,19].

HR-XRD data (Fig. 1) of the as-grown heterostructure reveal that the Ge epilayer was indeed pseudomorphic with respect to the $In_xGa_{1-x}As$ virtual substrate (VS). As shown by the symmetric (004) rocking curve (RC) in Fig. 1(a), the strain-induced compression of c_{Ge} was observed directly as an increase in the (004) Bragg angle of the ε-Ge film (blue). For comparison, the (004) RC from a quasi-lattice-matched Ge/GaAs heterostructure is also shown (red), emphasizing the resultant angular separation between the ε-Ge and relaxed Ge diffraction peaks due to strain incorporation. We note that the Pendellösung oscillations observed in the Ge/GaAs RC were not observed on the ε-Ge/$In_xGa_{1-x}As$ heterostructure, likely owing to disorder-induced x-ray scattering within the dislocation filtering $In_xGa_{1-x}As$ linearly graded buffer (LGB) and a thicker excitation volume in the relaxed Ge material rather than a non-abrupt ε-Ge/$In_xGa_{1-x}As$ heterointerface.

In addition, symmetric (004) and asymmetric (115) reciprocal space map (RSM) analysis permitted further characterization of the Ge epilayer strain-state, InAs mole fraction of the $In_xGa_{1-x}As$ VS, and relaxation state of the metamorphic buffer. Figs. 1(b) and 1(c) show the recorded (004) and (115) RSMs, respectively, highlighting the reciprocal lattice point (RLP) centroid for each layer. The Q_x–Q_z symmetry of the ε-Ge RLP suggests uniform crystallinity absent of mosaicity- or defect-related scattering, thereby implying a lack of observable relaxation with the ε-Ge epilayer. Likewise, the narrow, symmetric nature of the $In_xGa_{1-x}As$ VS RLP indicated dislocation-minimal constant composition epitaxy, signifying a strong confinement of lattice mismatch-induced defects in the metamorphic LGB and a high amount of buffer relaxation. These observations were quantified following the procedures outlined in Ref. [43,44], as summarily reported in Ref [25], yielding an $In_xGa_{1-x}As$ stressor InAs mole fraction, $x_{exp.}$, of 0.237. From the ~540 arcsec tilt determined *via* the (004) reflection, it can be posited that buffer relaxation occurred in a partially asymmetric nature [45], which was further confirmed *via* the presence of minute, but quantifiable asymmetries in the [1$\bar{1}$0] and [110]-oriented surface morphology of the ε-Ge/$In_{0.24}Ga_{0.76}As$ heterostructure (see Sec. I and Fig. S1 within the Supplemental Material [46]). Moreover, the Ge film was found to be 1.6% tensile strained with respect to relaxed (bulk) Ge, indicating a near-ideal stress transfer to the Ge lattice and reinforcing the nature of the ε-Ge RLP previously discussed.

Raman spectroscopic data (Fig. 2) further confirmed the nature of the ε-Ge epilayer strain, as demonstrated by the frequency shift observed in the measured ε-Ge/$In_{0.24}Ga_{0.76}As$

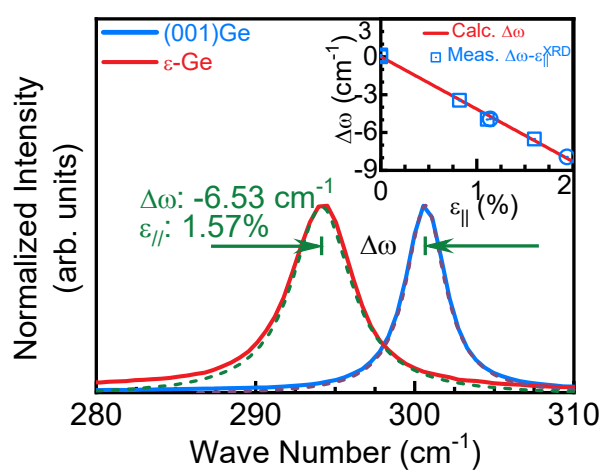

FIG. 2. Raman spectra collected from a (001)Ge substrate (blue) and the ε-Ge epilayer grown on $In_{0.24}Ga_{0.76}As$ (red). Inset highlights the relationship between the expected Raman wavenumber shift (solid line, red) and the HR-XRD-determined tensile strain (symbols, blue).

Raman spectra. As can be seen in Fig. 2, the ε-Ge epilayer (red) exhibited a wavenumber shift (Δω) of -6.53 cm^{-1} with respect to the Raman spectra taken from a (001)Ge substrate (blue), resulting in a strain value of $\varepsilon_{||}$ = 1.57% [50]. This value was found to be in good agreement with the theoretical misfit for the ε-Ge/$In_{0.24}Ga_{0.76}As$ heterostructure, $f \sim 1.63\%$. Additionally, the relationship between the measured Δω and XRD-determined strain ($\varepsilon_{||}^{XRD}$) is shown in the inset of Fig. 2. Also shown is the expected Raman shift as a function of strain (red) derived using the expression $\Delta\omega = -b\varepsilon_{||}$ cm^{-1} (see Sec. II of the Supplemental Material [46]). Inclusion of our previously reported results for ε-Ge/$In_xGa_{1-x}As$ heterostructures grown on GaAs (circles) [50] and Si (squares) [53] substrates revealed a strong correlation between the expected Δω deduced from $\varepsilon_{||}^{XRD}$ and the measured Raman shift (symbols), noting that experimental variance between the measured and expected values is likely due to minute strain anisotropies in the ε-Ge epilayers as a consequence of the slightly asymmetric nature of the $In_xGa_{1-x}As$ VS relaxation. These results therefore highlight the applicability of Raman strain analysis to the ε-Ge system across a wide-range of strain values and substrate platforms, and further reinforce the strain relaxation analysis *via* HR-XRD presented earlier.

Low-magnification TEM analysis (Fig. 3(a)) provided additional insight into the relaxation dynamics of the ε-Ge/$In_{0.24}Ga_{0.76}As$ heterostructure, revealing a dense network of misfit and threading dislocations (TDs) confined within the metamorphic $In_xGa_{1-x}As$ LGB. Likewise, high-magnification TEM analysis (Fig. 3(b)) demonstrated a highly uniform interface between the ε-Ge epilayer and $In_{0.24}Ga_{0.76}As$ strain template. We note that Fig. 3(b) consists of the as-recorded micrograph superimposed with a noise-filtered image of the same, the effect of which is to enhance image contrast in the vicinity of atomic columns. Utilization of this two-step Fast Fourier Transform (FFT) noise filtering approach (*i.e.*, $F^{-1}(F(k))$) suggested an atomically abrupt heterointerface lacking substantial atomic interdiffusion. In the proceeding section, we will provide definitive evidence for this conclusion *via* APT. More localized FFT patterns captured from representative 14 nm × 14 nm regions of the (i) ε-Ge epilayer, (ii) ε-Ge/$In_{0.24}Ga_{0.76}As$ heterointerface, and (iii), $In_{0.24}Ga_{0.76}As$ strain template are shown in Figs. 3(c)–3(e), respectively. The indistinguishable nature of the FFT patterns across the heterointerface and the absence of satellite reflections indicated the majority contribution of a single lattice parameter to the diffractogram, thereby providing ancillary support for a quasi-ideal pseudomorphic Ge epitaxy.

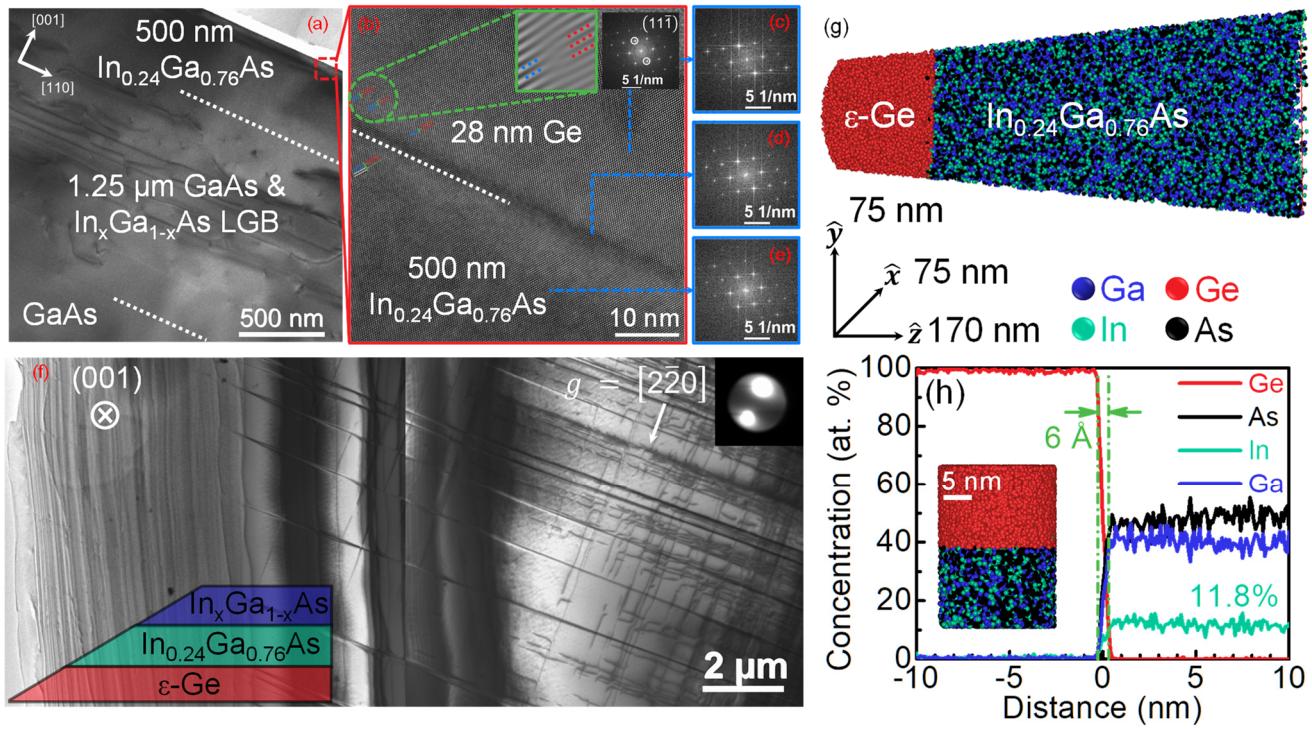

FIG. 3. (a) Low-magnification cross-sectional transmission electron micrograph (X-TEM) of the entire ε-Ge/$In_{0.24}Ga_{0.76}As$/$In_xGa_{1-x}As$/GaAs(001) heterostructure. (b) High-magnification X-TEM of the ε-Ge/$In_{0.24}Ga_{0.76}As$ heterointerface and (c)–(e) associated Fast Fourier Transform (FFT) patterns. Insets display the ⟨11$\bar{1}$⟩ crystallographic plane and corresponding reciprocal space reflections used in the misfit dislocation analysis. (f) Low-magnification plan-view TEM of a beveled ε-Ge/$In_{0.24}Ga_{0.76}As$ sample and corresponding representative cross-sectional schematic (bottom-left inset). (g) Reconstructed 3-D atom probe tomographic ion map of a representative 75 nm × 75 nm × 170 nm conical volume taken from the as-grown ε-Ge/$In_{0.24}Ga_{0.76}As$ heterostructure and (h) associated atomic concentration depth profile. The inset of (h) corresponds to the region from which the atomic concentration depth profile was generated.

Fig. 3(f) shows a plan-view TEM micrograph taken from a beveled sample foil (bottom-left inset) under the $g = (2\bar{2}0)$ diffraction condition. Utilizing plan-view TEM analysis permitted a conservative estimation of the TD density in the $In_{0.24}Ga_{0.76}As$ stressor, $\rho_{TDD} \leq 2\times10^7$ cm^{-2} (see Sec. III of the Supplemental Material [46]), noting that TDs were only observed upon etching of the ε-Ge epilayer. Additionally, Fig. 3(f) revealed an abrupt termination in the $In_{0.24}Ga_{0.76}As$ misfit dislocation (MD) network, which was posited to occur at the ε-Ge/$In_{0.24}Ga_{0.76}As$ heterointerface. This is conclusively demonstrated by FFT analysis of the {111} planes in the vicinity of the interface, as shown in the insets of Fig. 3(b). MDs exhibiting the insertion of an extra half-plane of atoms (*i.e.*, edge dislocations) were observed, noting that positive and negative edge dislocations were found in both the ε-Ge and $In_{0.24}Ga_{0.76}As$ stressor layers. Moreover, these MDs were confined to within 4 nm of the heterointerface and exhibited aperiodic MD spacing. Correlating these results with the previously-discussed HR-XRD analysis, the lack of quantifiable tilt in the (004) ε-Ge RLP (with respect to the $In_{0.24}Ga_{0.76}As$ stressor) suggests that these are 90° MDs. It is generally understood that under tensile strain, it is energetically favorable for perfect 60° dislocations to disassociate into leading 90° and trailing 30° partial dislocations (see Sec. III and Fig. S2 of the Supplementary Material) [46, 56]. Given the irregular MD spacing observed in Fig. 3(b) and the localization of MDs in ε-Ge to corresponding dislocations in the $In_{0.24}Ga_{0.76}As$ stressor, it is therefore likely that the observed MDs are 90° partial dislocations that formed during Ge epilayer growth. Indeed, a Burgers circuit traced around a representative dislocation core (Fig. S2(d)) revealed the formation of the stacking fault associated with the nucleation of a 90° partial dislocation having a projected Burgers vector of $(a_0/6)\langle 112\rangle$. Thus, as no quantifiable ρ_{TDD} was observed in the ε-Ge epilayer, we posit that the high strain energy at the Ge surface during growth resulted in enhanced TD glide at the ε-Ge/$In_{0.24}Ga_{0.76}As$ heterointerface, thereby preventing vertical TD propagation and accommodating strain relaxation through the formation and disassociation of perfect 60° MDs into leading 90° partial dislocations [60].

Lastly, independent corroboration of the ε-Ge/$In_{0.24}Ga_{0.76}As$ heterointerface abruptness was provided by APT, which was used to reconstruct atomically-accurate 3-D ion maps of representative 75 nm × 75 nm × 170 nm (conical) volumes of the as-grown ε-Ge/$In_{0.24}Ga_{0.76}As$ heterostructure. Fig. 3(g) shows one such reconstructed 3-D ion map, wherein individual gallium (Ga), indium (In), arsenic (As), and Ge atoms are depicted in blue, green, black, and red, respectively. Likewise, a magnified region in the vicinity of the ε-Ge/$In_{0.24}Ga_{0.76}As$ heterointerface (Fig. 3(h), inset) was used to generate a representative atomic concentration depth profile (Fig. 3(h)). Measurement of the separation between the 90% and 10% atomic thresholds for a given ion species allowed for estimation of the atomic interdiffusion at the ε-Ge/$In_{0.24}Ga_{0.76}As$ heterointerface. Explicitly, no quantifiable atomic interdiffusion occurred beyond an initial 6 Å diffuse region formed at the onset of Ge nucleation. This result can be explained by a combination of the low-temperature and low-growth rate Ge epitaxy conditions utilized in this work. The former is expected to minimize As surface desorption from the $In_xGa_{1-x}As$ surface prior to and during Ge nucleation, whereas the latter promotes uniform Ge surface coverage during nucleation and subsequent Frank–van der Merwe-dominated epitaxy. When taken together, these two processes reduce the likelihood of As out-diffusion into the growing Ge epilayer, consequently preserving heterointerfacial uniformity and abruptness. Finally, we note that the InAs mole fraction of the $In_xGa_{1-x}As$ virtual substrate as determined *via* APT analysis was 0.236 (11.8 atomic %), in excellent agreement with the HR-XRD results outlined earlier.

B. Electronic and Magnetotransport Properties of Highly-Tensile-Strained Ge

Having demonstrated the successful integration of highly-tensile-strained Ge on $In_xGa_{1-x}As$ strain templates, we now turn our attention toward the carrier dynamics of such heterostructures. To this end, the magnetotransport properties of the ε-Ge/$In_{0.24}Ga_{0.76}As$ heterostructure were measured in a van der Pauw configuration with magnetic

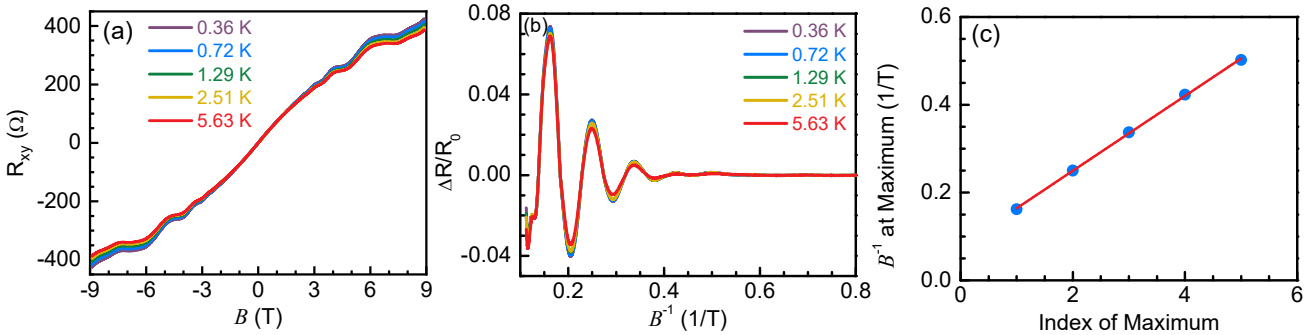

FIG. 4. (a) Transverse magnetoresistance (R_{XY} *vs* magnetic field, *i.e.*, Hall effect) obtained in a van der Pauw configuration over temperatures 0.36 K to 5.63 K and over magnetic fields ±9 T. Shubnikov–de Haas oscillations are visible at higher magnetic fields due to intermixing with longitudinal magnetoresistance. (b) The Shubnikov–de Haas oscillations plotted *vs* inverse magnetic field. (c) Inverse magnetic field (symbols, blue) at the maxima in (b) *vs* the index of the maxima, with a linear fit (solid line, red) displaying slope $S = 0.0853 \pm 0.001$ T^{-1}.

field B applied perpendicularly to the (001) growth direction and at temperatures ranging from 0.36 K to 5.63 K. Magnetotransport data consisted of transverse magnetoresistance ($R_{XY}(B)$, Hall effect) and longitudinal magnetoresistance. The latter was extracted by symmetrization of data obtained for the two polarities of B, since longitudinal magnetoresistance must be symmetric with respect to applied B. Fig. 4(a) presents $R_{XY}(B)$ *vs* B obtained at different measurement temperatures. From the slope of the linear region (over ± 2 T) an areal carrier density of $N_{S1} = 8.50\times10^{16}$ m^{-2} was deduced, which was substantially constant over the measured temperature range. The sign of the slope indicated that electrons were at the origin of this Hall effect. Additionally, Shubnikov–de Haas oscillations were observed at higher B, superimposed on the Hall effect and exhibiting a pronounced dependence on temperature. The Shubnikov–de Haas oscillations are observed in this van der Pauw geometry owing to mixing of $R_{XY}(B)$ with residual longitudinal magnetoresistance. As their origin lies in longitudinal magnetoresistance, the Shubnikov–de Haas oscillations could be extracted by symmetrization in B of the data. Fig. 4(b) shows the longitudinal magnetoresistance after the subtraction of a background to yield the oscillatory part (ΔR) and its subsequent normalization by the sheet resistance (R_0). The Shubnikov–de Haas oscillations exhibited a clear periodicity in inverse B, from which B^{-1} taken at the maxima *vs* the index of the maxima (arbitrarily starting with index 1 at $B = 0.16$ T^{-1}) is displayed in Fig. 4(c), resulting in a monotonic trend line with slope $S = 0.0853 \pm 0.001$ T^{-1}. An areal density N_{S2} was deduced from S [61,62], using the relation $N_{S2} = e/(\pi\hbar S)$, where e denotes the electron charge and $\hbar$ Planck's constant, yielding $N_{S2} = (5.67 \pm 0.06)\times10^{15}$ m^{-2}. Here we assumed negligible Zeeman splitting, and hence spin degeneracy. Whether the carriers giving rise to the Shubnikov–de Haas oscillations were electrons or holes could not be ascertained. Yet Shubnikov–de Haas oscillations require minimal broadening of Landau levels, implying that this carrier population (N_{S2}) had higher mobility than the population giving rise to the Hall effect (N_{S1}), which could not be detected in the Shubnikov-de Haas oscillations. From the dependence on temperature of the oscillations in Fig. 4(b), an effective mass was extracted using the so-called temperature term in the description of Shubnikov–de Haas oscillations [61–63]. It was found that this effective mass $m_2 = (0.049 \pm 0.007)\ m_e$, where m_e denotes the free-electron mass. From the magnetotransport measurements it was thus concluded that two carrier populations contributed to transport: an electron population with lower mobility and higher density ($N_{S1} = 8.50\times10^{16}$ m^{-2}), and a population of unknown type but with higher mobility and lower density ($N_{S2} = 5.67\times10^{15}$ m^{-2}) and with an effective mass $m_2 = (0.049 \pm 0.007)\ m_e$.

The extraction of the effective mass of the relatively higher mobility carriers was independently corroborated by way of electron cyclotron resonance (CR) analysis under high magnetic field. Fig. 5(a) displays the normalized transmission traces, T_B/T_0 at fixed magnetic fields ranging from 7 T to 17 T, as a function of energy, demonstrating the evolution of the effective mass. Broad resonances were observed as a result of the CR mobility of the carrier population being probed; however, extraction of the carrier effective mass as a function of the applied magnetic field, utilizing the measured resonance positions, was still possible, as shown in Fig. 5(b). The resulting effective mass at $B \approx 8$ T, $m^* = 0.056\ m_e$, was found to be in good agreement with that determined *via* the temperature dependence of the Shubnikov–de Haas oscillations. The increase in m^* with increasing B is due to the non-parabolicity effect in the conduction band of ε-Ge. Similar observations were reported in the literatures for several material systems [64-71] due to

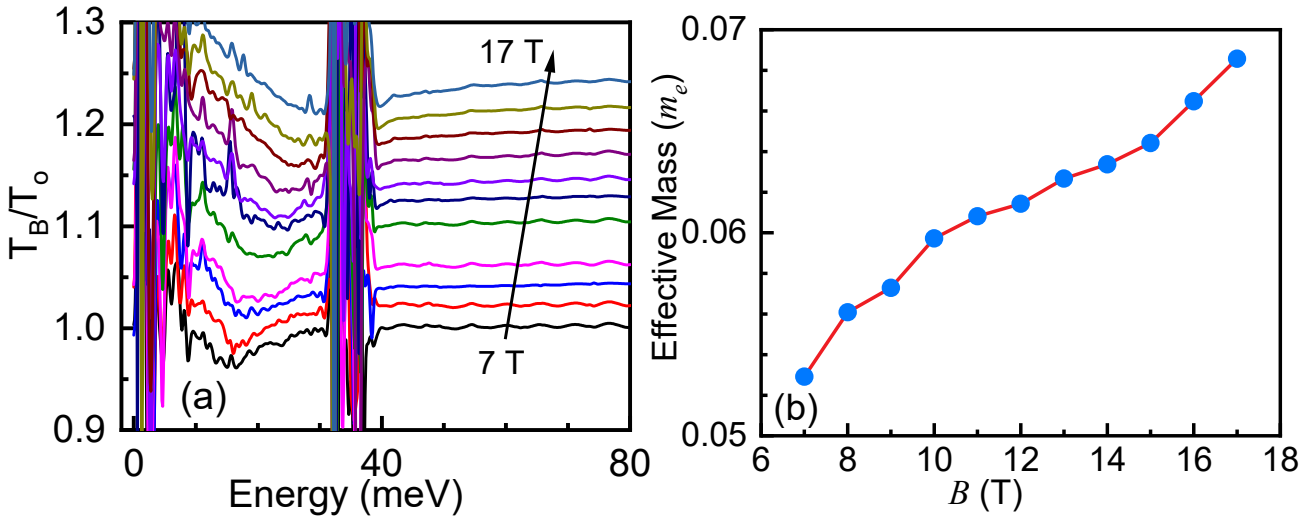

FIG. 5. (a) The normalized magneto-transmission traces, T_B/T_0 at fixed magnetic fields ranging from 7 T to 17 T, as a function of energy, noting that the traces have been shifted for clarity. (b) The evolution of effective mass as a function of magnetic field, extracted from the resonance positions of the CR measurements, taken at 4.5 K (line is a guide for the eye).

non-parabolicity in conduction band for *n*-type or valence band for *p*-type materials. However, neither measurement alone was sufficient to determine the carrier-type of the relatively higher mobility carriers. As such, electronic transport modeling of the ε-Ge/$In_xGa_{1-x}As$ material system was employed to provide additional insight into the empirical transport behavior.

C. Modelling of the Strain-Dependent Electronic Transport Properties of Ge

In order to clarify the origin of the Shubnikov–de Haas oscillations and carrier effective mass previously probed, the mobility in several ε-Ge/$In_xGa_{1-x}As$ heterostructures was calculated using a parametrization of the Boltzmann transport equation based on first-principles [20]. The temperature dependent Hall mobility measurements of unstrained and tensile strained Ge samples (*see* Table I) were performed using van der Pauw geometry to determine the carrier density and mobility of each sample. Fig. 6(a) shows the mobility calculated as a function of temperature for three different strain-states, corresponding to Ge grown on GaAs, $In_{0.16}Ga_{0.84}As$, and $In_{0.24}Ga_{0.76}As$ alloys, as compared to experiment. The carrier densities for these layers are ~ 4×10^{18} cm^{-3}, ~7×10^{18} cm^{-3}, and ~2×10^{18} cm^{-3}, respectively. The symbol in this figure represents the Hall mobiltiy data and the calculated solid lines are fitted to experimental results. In order to fit the experimetal data of Ge/AlAs sample (0% strain), a higher scattering rate for impurities was assumed since the measured mobility is quite low.

The *n*-type mobility ($N_e \approx 2\times10^{18}$ cm^{-3}) exhibited contributions from the *L* and Γ valleys in the ε-Ge region (1.6% ε-Ge/$In_{0.24}Ga_{0.76}As$), as well as the Γ valley in the $In_xGa_{1-x}As$ VS (Fig. 6(b)), noting that the contribution from each valley is proportional to the amplitude of the wave-

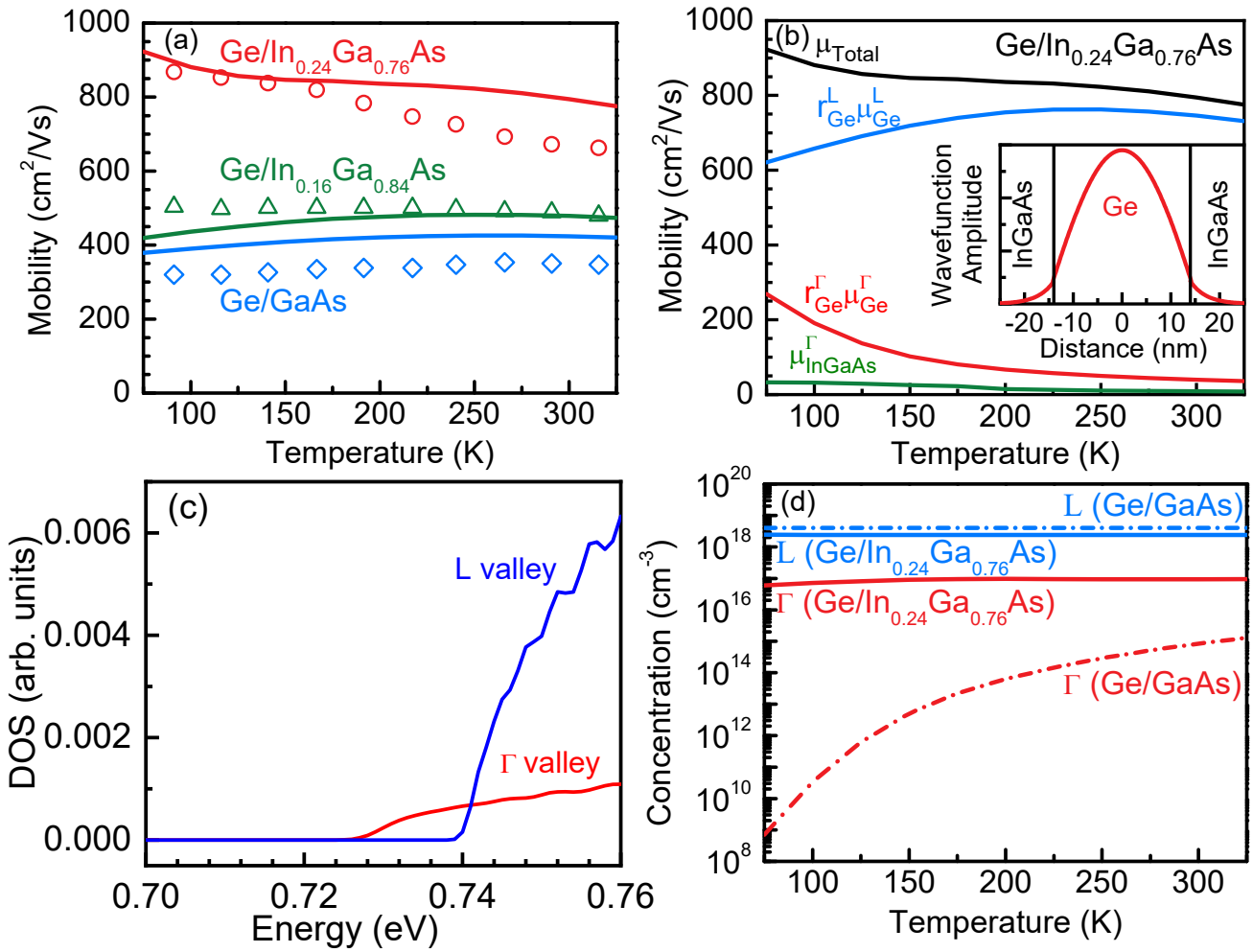

FIG. 6. (a) Measured (symbols) and calculated (solid lines) *n*-type mobility *vs* temperature in quantum-confined ε-Ge/$In_xGa_{1-x}As$ heterostructures for InAs mole fractions of 0, 0.16 and 0.24. The thicknesses of the Ge regions are: (i) 80 nm; (ii) 15 nm; and (iii), 30 nm, for the 0, 0.16, and 0.24 $In_xGa_{1-x}As$ alloys, respectively [25]. (b) Temperature dependence of the calculated contributions to the total mobility from the *L* and Γ valleys in the ε-Ge region and the Γ valley in the $In_{0.24}Ga_{0.76}As$ virtual substrate. The total mobility is given by $\mu_{Total} = \sum_j r_j \mu_j$, where $r_j = n_j / n_{Total}$ is the proportion of carriers in valley *j*. (c) Density of states (DOS) versus energy of *L* and Γ valleys, showing the higher DOS in *L* valley than and Γ valley. (d) Temperature dependence of the calculated volumetric carrier concentrations in the *L* and Γ valleys of ε-Ge and the Γ valley of $In_{0.24}Ga_{0.76}As$ for the 1.6% ε-Ge/$In_{0.24}Ga_{0.76}As$ heterostructure.

function (of the corresponding valley) in each region. For biaxial tensile strains lower than 1.6%, all conduction was found to occur *via* the L valley in Ge. At strain-states above 1.6%, contribution from the Γ valley was found to increase, particularly at low (< 150 K) temperatures. Fig. 6(b) shows the contribution from each valley to the total mobility in the 1.6% ε-Ge/$In_{0.24}Ga_{0.76}As$ heterostructure. While transport primarily occurred *via* the L valley, at T = 100 K, the contribution of Γ valley transport to the total mobility increased to 17%, diminishing with increasing temperature to approximately 3% at T = 300 K. These results can be explained by the much larger density of states within the L valley (*i.e.*, the DOS masses of the L and Γ valleys are $m_L^{DOS} = 0.22\, m_e$ and $m_\Gamma^{DOS} = 0.05\, m_e$, respectively), which became increasingly populated with rising temperature. Fig. 6(c) shows the calculated DOS versus energy in both L and Γ valleys under 1.6% tensile strain. One can find from this figure that the DOS in Γ valley is lower than that of L valley and most of the carriers will still reside within the L valley. Additionally, in spite of the high electron mobility of the $In_{0.24}Ga_{0.76}As$ VS, it contributed comparatively little to the total mobility, owing to wave-function confinement within the ε-Ge region (Fig. 6(b), inset). However, due to the smaller DOS of the Γ valley in Ge, such quantum confinement tended to decrease the mobility contribution of Γ valley carriers to the total electron mobility, as compared to carriers residing in the higher DOS L valley in Ge. At room temperature, the carriers will populate both valleys with more at the L valley than Γ valley due to higher DOS. The two ways one can increase the carrier density in the Γ valley: (i) by injecting carriers from the L valley by incorporating doping in the ε-Ge layer or (ii) during lasing process by electrical injection [72].

Relating the transport modeling results to the aforementioned magnetotransport analysis, it was found that the measured electron population having a higher density (N_{S1} =8.50×10^{16} m^{-2}) corresponds well to L valley electron conduction in ε-Ge, whereas the lower population density carriers (N_{S2} = 5.67×10^{15} m^{-2}), exhibiting an effective mass m_2 = (0.049 ± 0.007) m_e, represented Γ valley electron conduction in ε-Ge. Comparison of the calculated carrier populations in the L and Γ valleys of Ge and $In_xGa_{1-x}As$ as a function of temperature (Fig. 6(d)) yielded qualitative agreement with the empirical magnetotransport data. Moreover, calculation of the Γ valley transport effective mass in 1.6% ε-Ge (Fig. 7) revealed excellent agreement between the effective masses of the first two quantum sublevels (0.045 m_e and 0.051 m_e, respectively), and that measured by experiment. As such, it can thus be posited that the effective mass of the relatively higher mobility carriers probed *via* the magnetotransport and CR studies corresponds to electrons residing in the first two energy levels of the Γ valley in ε-Ge. Taken as a whole, however, these results indicate that ε > 1.6% is likely necessary in order to increase Γ valley occupancy and therefore enhance the Γ valley contribution to the total ε-Ge mobility.

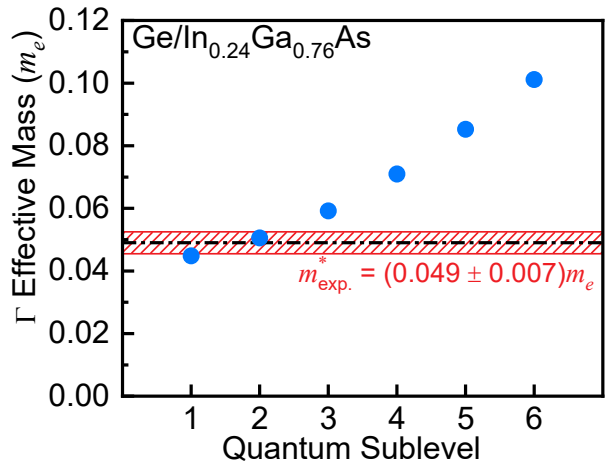

FIG. 7. Evolution of the ε-Ge Γ valley effective mass with increasing quantum sublevel for the 1.6% ε-Ge/$In_{0.24}Ga_{0.76}As$ heterostructure at T = 0 K.

IV. CONCLUSIONS

To summarize, we have provided fundamental insight into the nature of electronic transport in highly tensile strained Ge materials along with their detailed structural analysis by x-ray, Raman, and cross-sectional and plan-view transmission electron microscopic study. The quantification of defects and surface roughness were provided in supplementary material. The presented magnetotransport and cyclotron resonance results, when coupled with our first-principles-parameterized Boltzmann transport modeling, revealed the strain-dependence of L and Γ valley conduction in tensile strained Ge. The temperature dependence of the calculated mobility and carrier contributions in each valley of 1.6% ε-Ge were decoupled based on the experimental Hall measurement results, and most of the carriers will reside within the L valley due to higher density of states. In addition, the effective mass, $m^* \approx 0.056\, m_e$ determined *via* cyclotron resonance was in agreement with Shubnikov–de Haas oscillations. Moreover, the temperature-dependent competitiveness between L and Γ valley conduction in tensile strained Ge has significant importance for future electron devices, such as strained Ge-based gate-all-around nanowire FETs [13,15] and tunnel FETs [19, 24], wherein epitaxial strain is a key mechanism for improving carrier mobility and device drive current. Our results, however, are not limited to Ge-based electronics, as we also demonstrate the first direct experimental probing of the electron effective mass in Ge under high strain, thereby allowing for comparison with current and previous theoretical results [11,17–19].

ACKNOWLEDGEMENTS

M. C. acknowledges financial support from the NSF under grant number ECCS-1348653. M. H. acknowledges partial support from the NSF under grant number ECCS-

ECCS-2042079, a US-Ireland joint R&D program. G. A. K. acknowledges the support of the Air Force Office of Scientific Research under award number FA9550-17-1-0341. F. M.–A. acknowledges the financial support of the US-Ireland R&D Partnership Program by Science Foundation Ireland (SFI) Grant No. SFI/14/US/I3057. The authors also acknowledge the NCFL-Institute for Critical Technology and Applied Science and Virginia Tech Nanofabrication for providing materials characterization facilities. M. C. and M. H. would also like to acknowledge Dr. Patrick Goley for assisting with the TEM imaging. Lastly, a portion of this work was performed at the National High Magnetic Field Laboratory, which is supported by the National Science Foundation Cooperative Agreement No. DMR-1157490 and the State of Florida.

---

*Corresponding author.
mantu.hudait@vt.edu
philip.murphy@tyndall.ie

[1] T. Ghani, M. Armstrong, C. Auth, M. Bost, P. Charvat, G. Glass, T. Hoffmann, K. Johnson, C. Kenyon, J. Klaus *et al*., A 90nm High Volume Manufacturing Logic Technology Featuring Novel 45nm Gate Length Strained Silicon CMOS Transistors, IEEE Int. Electron Devices Meet. (IEDM) (2003), pp. 11.6.1-11.6.3

[2] C. -H. Ge, C. -C. Lin, C. -H. KO, C. -C. Huang, Y. -C. Huang, B. -W. Chan, B. -C. Pemg, C. -C. Sheu, P. -Y. Tsai, L. -G. Yao *et al*., Process-Strained Si (PSS) CMOS Technology Featuring 3D Strain Engineering, IEEE Int. Electron Devices Meet. (IEDM) (2003), pp. 3.7.1-3.7.4.

[3] S. E. Thompson, M. Armstrong, C. Auth, M. Alavi, M. Buehler, R. Chau, S. Cea, T. Ghani, G. Glass, T. Hoffman *et al*., A 90-nm Logic Technology Featuring Strained-Silicon, IEEE Trans. Electron Devices **51**, 1790 (2004).

[4] Q. Ouyang, M. Yang, J. Holt, S. Panda, H. Chen, H. Utomo, M. Fischetti, N. Rovedo, J. Li; N. Klymko *et al*., Investigation of CMOS Devices with Embedded SiGe Source/Drain on Hybrid Orientation Substrates, Symp. VLSI Technol. Tech. Dig. (2005), pp. 28-29.

[5] D. K. Nayak, K. Goto, A. Yutani, J. Murota, and Y. Shiraki, High-Mobility Strained-Si PMOSFET's, IEEE Trans. Electron Devices **43**, 1709 (1996).

[6] R. Chau, B. Doyle, S. Datta, J. Kavalieros, and K. Zhang, Integrated Nanoelectronics for the Future, Nat. Mater. **6**, 810 (2007).

[7] R. Pillarisetty, Academic and Industry Research Progress in Germanium Nanodevices, Nature **479**, 324 (2011).

[8] M. Heyns, A. Alian, G. Brammertz, M. Caymax, Y. C. Chang, L. K. Chu, B. De Jaeger, G. Eneman, F. Gencarelli, G. Groeseneken *et al*., Advancing CMOS Beyond the Si Roadmap with Ge and III/V Devices, IEEE Int. Electron Devices Meet. (IEDM) (2011), pp. 13.1.1-13.1.4.

[9] K. J. Kuhn, Considerations for Ultimate CMOS Scaling, IEEE Trans. Electron Devices **59**, 1813 (2012).

[10] P. D. Nguyen, M. B. Clavel, P. S. Goley, J. –S. Liu, N. P. Allen, L. J. Guido, and M. K. Hudait, Heteroepitaxial Ge MOS Devices on Si Using Composite AlAs/GaAs Buffer, IEEE J. Electron Devices Soc. **3**, 341 (2015).

[11] M. V. Fischetti and S. E. Laux, Band Structure, Deformation Potentials, and Carrier Mobility in Strained Si, Ge, and SiGe Alloys, J. Appl. Phys. **80**, 2234 (1996).

[12] J. Kim and M. V. Fischetti, Electronic Band Structure Calculations for Biaxially Strained Si, Ge, and III–V Semiconductors, J. Appl. Phys. **108**, 013710 (2010).

[13] W. Chern, P. Hashemi, J. T. Teherani, T. Yu, Y. Dong, G. Xia, D. A. Antoniadis, and J. L. Hoyt, High Mobility High-κ-All-Around Asymmetrically Strained Germanium Nanowire Trigate p-MOSFETs, IEEE Int. Electron Devices Meet. (IEDM) (2012), pp. 16.5.1-16.5.4.

[14] A. Agrawal, M. Barth, G. B. Rayner, V. T. Arun, C. Eichfeld, G. Lavallee, S. -Y. Yu, X. Sang, S. Brookes, Y. Zheng *et al*., Enhancement Mode Strained (1.3%) Germanium Quantum Well FinFET (W_{Fin}=20nm) with High Mobility (μ_{Hole}=700 cm^2/Vs), Low EOT (~0.7nm) on Bulk Silicon Substrate, IEEE Int. Electron Devices Meet. (IEDM) (2014), pp. 16.4.1-16.4.4.

[15] L. Witters, H. Arimura, F. Sebaai, A. Hikavyy, A. P. Milenin, R. Loo, A. De Keersgieter, G. Eneman, T. Schram, K. Wostyn *et al*., Strained Germanium Gate-All-Around pMOS Device Demonstration Using Selective Wire Release Etch Prior to Replacement Metal Gate Deposition, IEEE Trans. Electron Devices **64**, 4587 (2017).

[16] K. Wang, Q. Gong, H. Zhou, C. Kang, J. Yan, Q. Liu, and S. Wang, Mobility Enhancement in Tensile-Strained Ge Grown on InAlP Metamorphic Templates, Appl. Surf. Sci. **291**, 45 (2014).

[17] D. Rideau, M. Feraille, L. Ciampolini, M. Minondo, C. Tavernier, H. Jaouen, and A. Ghetti, Strained Si, Ge, and $Si_{1-x}Ge_x$ Alloys Modeled with a First-Principles-Optimized Full-Zone **k·p** Method, Phys. Rev. B **74**, 195208 (2006).

[18] M. El Kurdi, G. Fishman, S. Sauvage, and P. Boucaud, Band Structure and Optical Gain of Tensile-Strained Germanium Based on a 30 Band **k·p** Formalism, J. Appl. Phys. **107**, 013710 (2010).

[19] K. -H. Kao, A. S. Verhulst, M. Van de Put, W. G. Vandenberghe, B. Soree, W. Magnus, and K. De Meyer, Tensile Strained Ge Tunnel Field-Effect Transistors: **k·p** Material Modeling and Numerical

Device Simulation, J. Appl. Phys. **115**, 044505 (2014).

[20] F. Murphy-Armando and S. Fahy, Giant Enhancement of *n*-type Carrier Mobility in Highly Strained Germanium Nanostructures, J. Appl. Phys. **109**, 113703 (2011).

[21] M. K. Hudait, F. Murphy-Armando, D. Saladukha, M. B. Clavel, P. S Goley, D. Maurya, S. Bhattacharya, and T. J. Ochalski, Design, Theoretical and Experimental Investigation of Tensile-strained Germanium Quantum-well Laser Structure, ACS Appl. Electron. Mater. **10**, 4535-4547 (2021).

[22] D. Saladukha, M. B. Clavel, F. Murphy-Armando, G. Greene-Diniz, M. Gruening, M. K. Hudait, and T. J. Ochalski, Direct and indirect band gaps in Ge under biaxial tensile strain investigated by photoluminescence and photoreflectance studies, Phys. Rev. B **97**, 195304 (2018).

[23] M. K. Hudait, M. Clavel, L. Lester, D. Saladukha, T. Ochalski, and F. Murphy-Armando, Heterogeneously grown tunable group-IV laser on silicon, *Proc. SPIE 9755, Quantum Sensing and Nano Electronics and Photonics XIII, 97550Y* (February 13, **2016**).

[24] J. -S. Liu; M. B. Clavel, and M. K. Hudait, Performance Evaluation of Novel Strain-Engineered Ge-InGaAs Heterojunction Tunnel Field-Effect Transistors, IEEE Trans. Electron Devices **62**, 3223 (2015).

[25] M. Clavel, P. Goley, N. Jain, Y. Zhu, and M. K. Hudait, Strain-Engineered Biaxial Tensile Epitaxial Germanium for High-Performance Ge/InGaAs Tunnel Field-Effect Transistors, IEEE J. Electron Dev. Soc. **3**, 184 (2015).

[26] J. -S. Liu, M. Clavel, and M. K. Hudait, An Energy-Efficient Tensile-Strained Ge/InGaAs TFET 7T SRAM Cell Architecture for Ultra-low Voltage Applications, IEEE Trans. Electron Devices **64**, 2193 (2017).

[27] J. -S. Liu, M. Clavel, and M. K. Hudait, TBAL: Tunnel FET-Based Adiabatic Logic for Energy-Efficient, Ultra-Low Voltage IoT Applications, IEEE J. Electron Dev. Soc. **7**, 210 (2019).

[28] S. Bao, D. Kim, C. Onwukaeme, S. K Gupta, K. Saraswat, K. H. Lee, Y. Kim, D. Min, Y. Jung, H. Qiu *et al*., Low-threshold optically pumped lasing in highly strained germanium nanowires, Nature Communication **8**, 1845 (2017).

[29] S. Gupta, D. Nam, J. Vuckovic, and K. Saraswat, Room temperature lasing unraveled by a strong resonance between gain and parasitic absorption in uniaxially strained germanium, Phys. Rev. B **97**, 155127 (2018).

[30] J. Petykiewicz, D. Nam, D. S. Sukhdeo, S. Gupta, S. Buckley, A. Y. Piggott, J. Vučković, and K. C. Saraswat, Direct bandgap light emission from strained germanium nanowires coupled with high-Q nanophotonic cavities, Nano Lett. **16**, 2168-2173 (2016).

[31] C. Morrison and M. Myronov, Strained germanium for applications in spintronics, Physica Status Solidi (A): Applications and Materials **213**, 2809 (2016).

[32] L. A. Terrazos, E. Marcellina, Z. Wang, S. N. Coppersmith, M. Friesen, A. R. Hamilton, X. Hu, B. Koiller, A. L. Saraiva, D. Culcer *et al.,* Theory of hole-spin qubits in strained germanium quantum dots, Phys. Rev. B **103**, 12 (2021).

[33] A. Sammak, D. Sabbagh, N. W. Hendrickx, M. Lodari, B. P. Wuetz, A. Tosato, L. Yeoh, M. Bollani, M. Virgilio, M. A. Schubert *et al*., Shallow and Undoped Germanium Quantum Wells: A Playground for Spin and Hybrid Quantum Technology, Adv. Functional Materials **29**, 1807613 (2019).

[34] Y. Bai, K. E. Lee, C. Cheng, M. L. Lee, and E. A. Fitzgerald, Growth of Highly Tensile-Strained Ge on Relaxed $In_xGa_{1-x}As$ by Metal-Organic Chemical Vapor Deposition, J. Appl. Phys. **104**, 084518 (2008).

[35] R. Jakomin, M. de Kersauson, M. El Kurdi, L. Largeau, O. Mauguin, G. Beaudoin, S. Sauvage, R. Ossikovski, G. Ndong, M. Chaigneau *et al*., High Quality Tensile-Strained *n*-doped Germanium Thin Films Grown on InGaAs Buffer Layers by Metal-Organic Chemical Vapor Deposition, Appl. Phys. Lett. **98**, 091901 (2011).

[36] F. Murphy–Armando and S. Fahy, First-principles Calculation of Carrier-Phonon Scattering in *n*-type $Si_{1-x}Ge_x$ Alloys, Phys. Rev. B **78**, 035202 (2008).

[37] F. Murphy-Armando, Enhancement of the Electronic Thermoelectric Properties of Bulk Strained Silicon-Germanium Alloys Using the Scattering Relaxation Times from First-Principles Calculations, J. Appl. Phys. **126**, 215103 (2019).

[38] C. Jacoboni and L. Reggiani, The Monte Carlo Method for the Solution of Charge Transport in Semiconductors with Applications to Covalent Materials, Rev. Mod. Phys. **55**, 645 (1983).

[39] D. Chattopadhyay and H. Queisser, Electron Scattering by Ionized Impurities in Semiconductors, Rev. Mod. Phys. **53**, 745 (1981).

[40] R. Barrie, Electronic Conduction in Solids with Spherically Symmetric Band Structure, Proc. Phys. Soc. B **69**, 553 (1956).

[41] Y. A. Goldberg and N. M. Schmidt, *Handbook Series on Semiconductor Parameters* (World Scientific, London, 1999), Vol. II, p. 62–88.

[42] N. Pavarelli, T. J. Ochalski, F. Murphy-Armando, Y. Huo, M. Schmidt, G. Huyet, and J. S. Harris, Optical Emission of a Strained Direct-Band-Gap Ge Quantum Well Embedded Inside InGaAs Alloy Layers, Phys. Rev. Lett. **110**, 177404 (2013).

[43] J. –M. Chauveau, Y. Androussi, A. Lefebvre, J. Di Persio, and Y. Cordier, Indium Content Measurements in Metamorphic High Electron

Mobility Transistor Structures by Combination of X-ray Reciprocal Space Mapping and Transmission Electron Microscopy, J. Appl. Phys. **93**, 4219 (2003).

[44] M. K. Hudait, Y. Lin, and S. A. Ringel, Strain Relaxation Properties of $InAs_yP_{1-y}$ Metamorphic Materials Grown on InP Substrates, J. Appl. Phys. **105**, 061643 (2009).

[45] R. S. Goldman, H. H. Wieder, and K. L. Kavanagh, Correlation of Anisotropic Strain Relaxation with Substrate Misorientation Direction at InGaAs/GaAs(001) Interfaces, Appl. Phys. Lett. **67**, 344 (1995).

[46] See the Supplemental Material online for extended discussions on the ε-Ge/$In_{0.24}Ga_{0.76}As$ heterostructure's surface morphological properties, Raman spectroscopy analysis methodology, and TEM dislocation identification methodology.

[47] A. M. Andrews, A. E. Romanov, J. S. Speck, M. Bobeth, and W. Pompe, Development of Cross-Hatch Morphology During Growth of Lattice Mismatched Layers, Appl. Phys. Lett. **77**, 3740 (2000).

[48] A. M. Andrews, J. S. Speck, A. E. Romanov, M. Bobeth, and W. Pompe, Modeling Cross-Hatch Surface Morphology in Growing Mismatched Layers. J. Appl. Phys. **91**, 1933 (2002).

[49] M. Natali, F. Romanato, E. Napolitani, D. De Salvador, and A. V. Drigo, Lattice Curvature Generation in Graded $In_xGa_{1-x}As$/GaAs Buffer Layers, Phys. Rev. B **62**, 11054 (2000).

[50] M. B. Clavel and M. K. Hudait, Band Offset Enhancement of *a*-Al_2O_3/Tensile-Ge for High Mobility Nanoscale pMOS Devices, IEEE Electron Device Lett. **38**, 1196 (2017).

[51] E. Anastassakis and M. Cardona, *High Pressure in Semiconductor Physics II* (Academic Press, San Diego, 1998), Vol. 55, Ch. 3.

[52] Z. Sui and I. P. Herman, Effect of Strain on Phonons in Si, Ge, and Si/Ge Heterostructures, Phys. Rev. B **48**, 17938 (1993).

[53] M. Clavel, D. Saladukha, P. S. Goley, T. J. Ochalski, F. Murphy-Armando, R. J. Bodnar, and M. K. Hudait, Heterogeneously-Grown Tunable Tensile Strained Germanium on Silicon for Photonic Devices, ACS Appl. Mater. Interfaces **7**, 26470 (2015).

[54] O. Madelung, *Semiconductors: Intrinsic Properties of Group IV Elements and III-V, II-VI, and I-VII Compounds* (Springer, Berlin, 1985), Vol. 22a.

[55] Y. -Y. Fang, J. Tolle, R. Roucka, A. V. G. Chizmeshya, J. Kouvetakisa, V. R. D'Costa, and J. Menéndez, Perfectly Tetragonal, Tensile-Strained Ge on $Ge_{1-y}Sn_y$ Buffered Si(100), Appl. Phys. Lett. **90**, 061915 (2007).

[56] J. Petruzzello and M. R. Leys, Effect of the Sign of Misfit Strain on the Dislocation Structure at Interfaces of Heteroepitaxial $GaAs_xP_{1-x}$ Films, Appl. Phys. Lett. **53**, 2414 (1988).

[57] J. Ayers, *Heteroepitaxy of Semiconductors: Theory, Growth, and Characterization* (CRC Press, Boca Raton, 2007), p. 36–67, Ch. 5.

[58] A. F. Marshall, D. B. Aubertine, W. D. Nix, and P. C. McIntyre, Misfit Dislocation Dissociation and Lomer Formation in Low Mismatch SiGe/Si Heterostructures, J. Mater. Res. **20**, 447 (2005).

[59] H. Gottschalk, Motion of Partial Dislocations, J. Phys. Colloques **40**, 127 (1979).

[60] N. A. El-Masry, J. C. Tarn, and N. H. Karam, Interactions of Dislocations in GaAs Grown on Si Substrates with InGaAs-GaAsP Strained Layer Superlattices, J. Appl. Phys. **64**, 3672 (1988).

[61] C. Morrison and M. Myronov, Electronic Transport Anisotropy of 2D Carriers in Biaxial Compressive Strained Germanium, Appl. Phys. Lett. **111**, 192103 (2017).

[62] R. Pisoni, A. Kormányos, M. Brooks, Z. Lei, P. Back, M. Eich, H. Overweg, Y. Lee, P. Rickhaus, K. Watanabe *et al*., Interactions and Magnetotransport through Spin-valley Coupled Landau Levels in Monolayer MoS_2, Phys. Rev. Lett. **121**, 247701 (2018).

[63] P. T. Coleridge, Small-angle Scattering in Two-dimensional Electron Gases, Phys. Rev. B **44**, 3793 (1991).

[64] M. J. Yang, P. J. Lin-Chung, R. J. Wagner, J. R. Waterman, W. J. Moore, and B. V. Shanabrook, Far-infrared spectroscopy in strained AlSb/InAs/AlSb quantum wells, Semicond. Sci. Technol. **8**, S129 (1993).

[65] V. Y. Aleshkin, V. I. Gavrilenko, A. V. Ikonnikov, Y. G. Sadofyev, J. P. Bird, S. R. Johnson, and Y. -H. Zhang, Cyclotron Resonance in Doped and Undoped InAs/AlSb Heterostructures with Quantum Wells, Semiconductors **39**, 62-66 (2005).

[66] T. E. Whall, A. D. Plews, N. L. Mattey, P. J. Phillips, and U. Ekenberg, Effective mass and band nonparabolicity in remote doped Si/$Si_{0.8}Ge_{0.2}$ quantum wells, Appl. Phys. Lett. **66**, 2724 (1995).

[67] G. C. Osbourn, J. E. Schirber, T. J. Drummond, L. R. Dawson, B. L. Doyle, and I. J. Fritz, Large valence-band nonparabolicity and tailorable hole masses in strained-layer superlattices, Appl. Phys. Lett. **49**, 731 (1986).

[68] O. Drachenko, D. V. Kozlov, V. Y. Aleshkin, V. I. Gavrilenko, K. V. Maremyanin, A. V. Ikonnikov, B. N. Zvonkov, M. Goiran, J. Leotin, G. Fasching *et al*., High-field splitting of the cyclotron resonance absorption in strained p-InGaAs/GaAs quantum wells, *Phys. Rev.* B **79**, 073301 (2009).

[69] J. E. Schirber, I. J. Fritz, and L. R. Dawson, Light-hole conduction in InGaAs/GaAs strained-layer superlattices, Appl. Phys. Lett. **46**, 187 (1985).

[70] N. Tang, B. Shen, M. J. Wang, Z. J. Yang, K. Xu, G. Y. Zhang, T. Lin, B. Zhu, W. Z. Zhou, and J. H. Chu,

Influence of the magnetic field on the effective mass of the two-dimensional electron gas in $Al_xGa_{1-x}N$/GaN heterostructures, phys. stat. sol. (c) **3**, 2246-2249 (2006).

[71] Y. H. Park, H. C. Koo, K. H. Kim, H. Kim, J. Chang, and S. H. Han, Influence of the magnetic field on the effective mass and the Rashba effect in an $In_{0.53}Ga_{0.47}As$ quantum-well structure, J. Korean Phys. Soc. **57**, 1929-1932 (2010).

[72] "*Photonics and Electronics with Germanium*", Kazumi Wada (Editor), Lionel C. Kimerling (Editor), Wiley-VCH, **2015**. Chapter 12, pp. 267-303.